BioMedInformatics

MDPI

Article

Identification of Ferroptosis-Related Grade-Discriminative Biomarkers and a Prognostic Signature in Glioma via Integrative Machine Learning and Single-Cell Analyses

Mengnan Wang [1,2], Tianci Wu [1,2] and Daming Wang [1,*]

[1] Department of Neurosurgery, Beijing Hospital, National Center of Gerontology, Institute of Geriatric Medicine, Chinese Academy of Medical Sciences, Beijing 100730, China; moralewance@163.com (M.W.)
[2] Fifth School of Clinical Medicine, Peking University, Beijing 100730, China
* Correspondence: damingbjh@163.com

Abstract

Glioma is the most common primary malignant brain tumor, with glioblastoma (GBM) carrying a 5-year survival rate below 10%. We analyzed 693 CGGA expression profiles, including 692 samples with available WHO grade (249 GBM and 443 lower-grade glioma [LGG]). WGCNA used all 693 profiles, whereas grade-dependent differential expression and machine-learning screening used the 692 grade-labeled samples. Screening-stage five-fold cross-validation identified ElasticNet as the numerically highest-performing reference model (AUC = 0.852), although Random Forest and Ridge performed nearly identically and yielded 12 core grade-discriminative biomarkers (ALOX15, TFRC, GCLC, DPP8, MBOAT2, NCOA4, NOX5, PIK3CB, CISD2, AMD1, TFR2, TRAF6). After panel selection, a 12-gene ElasticNet model fitted only in a reproducible stratified training set (n = 486) achieved an AUC of 0.847 (95% CI 0.790–0.896) in the internal test set (n = 206); because upstream feature discovery preceded the split, this internal estimate may remain optimistic. The fixed cross-platform subset achieved an AUC of 0.775 in the independent GSE16011 cohort. Virtual knockout (scTenifoldKnk) identified convergent perturbation of a stemness-associated program (SOX2, NES, PTPRZ1, TCF4) downstream of TFRC, GCLC, and TRAF6, and reanalysis of public CRISPR-Cas9 screening data (DepMap, 67 glioma cell lines) showed dependency signals for NCOA4 (49% of lines) and TFRC (24%). A LASSO-Cox risk score stratified patients with significant survival differences (HR = 3.75; time-dependent AUC 0.741–0.791) and independent prognostic value (multivariate HR = 2.02). These results support a biologically coherent ferroptosis-related panel while emphasizing the need for prospective validation.

Keywords: glioma; ferroptosis; grade-discriminative biomarkers; machine learning; WGCNA; single-cell; virtual knockout; prognostic risk score; Scissor

Check for updates

Academic Editors: Alexandre G. De Brevern, Saurav Mallik, Priyanka Roy and Zhongming Zhao

Received: 5 July 2026
Revised: 27 August 2026
Accepted: 30 September 2026
Published: 6 October 2026

Copyright: © 2026 by the authors. Licensee MDPI, Basel, Switzerland. This article is an open access article distributed under the terms and conditions of the Creative Commons Attribution (CC BY) license.

1. Introduction

Gliomas represent the most common and aggressive primary brain tumors in adults. Glioblastoma (GBM, WHO grade IV) carries a 5-year survival rate of less than 10% despite maximal multimodal therapy including surgical resection, radiotherapy, and temozolomide chemotherapy [1,2]. The discovery of isocitrate dehydrogenase (IDH) mutations has fundamentally reshaped glioma classification, with IDH-mutant lower-grade gliomas (LGG) following a more indolent clinical course compared to IDH-wildtype GBM [3].

However, the molecular mechanisms underlying glioma progression and the identification of reliable grade-discriminative biomarkers remain pressing clinical needs.

Ferroptosis is a form of regulated cell death driven by iron-dependent accumulation of lipid peroxides, distinct from apoptosis, necroptosis, and autophagy [4,5]. It is characterized by glutathione (GSH) depletion, inactivation of glutathione peroxidase 4 (GPX4), and subsequent accumulation of lipid reactive oxygen species [6]. Ferroptosis has been increasingly implicated in cancer pathogenesis, including glioma, where iron metabolism dysregulation and oxidative stress are hallmarks of the tumor microenvironment [7,8]. Several ferroptosis-related gene signatures have been constructed for glioma prognosis prediction, including the ferroptosis-related gene prognostic index (FRGPI; HMOX1, TFRC, JUN, SOCS1) [9], 11-gene ferroptosis signatures [10], and hypoxia-induced ferroptosis models [11]. However, these signatures predominantly focused on prognostic stratification rather than grade discrimination, and their gene compositions showed limited overlap, suggesting that the ferroptosis gene landscape in glioma remains incompletely characterized.

The tumor microenvironment (TME) of glioma is profoundly shaped by immune cell infiltration, with tumor-associated macrophages (TAMs) constituting the most abundant immune population [12–14]. Ferroptosis and immune regulation are tightly interconnected: ferroptotic cells release damage-associated molecular patterns (DAMPs) that modulate dendritic cell maturation and T-cell activation [15], and CD8+ T-cell-derived interferon-γ can promote ferroptosis through SLC7A11 downregulation [16]. Conversely, ferroptosis resistance mechanisms, including the NRF2 antioxidant pathway and the FSP1-CoQ_{10} axis, have been linked to immunosuppressive TME remodeling [17,18]. Despite this mechanistic interplay, the grade-discriminative value of ferroptosis-related genes in the context of the glioma immune microenvironment has not been systematically investigated.

Single-cell RNA sequencing (scRNA-seq) has enabled unprecedented resolution of cellular heterogeneity in glioma, revealing distinct functional states of malignant cells and TAMs [19,20]. Recently, computational tools for in silico gene perturbation—such as scTenifoldKnk—have emerged as powerful approaches to predict gene function from scRNA-seq data without experimental knockout [21]. These methods construct gene regulatory networks (GRNs) from single-cell transcriptomes and simulate gene knockout by removing target gene edges, thereby identifying downstream perturbed pathways. In parallel, interpretable machine-learning frameworks that integrate brain imaging and survival data have highlighted the value of combining high-dimensional molecular features with clinical outcomes [22]. Their application to ferroptosis gene function prediction in glioma represents an unexplored opportunity, and recent work on artificial-intelligence-guided nanocarrier design further illustrates the growing role of computational screening in precision medicine [23].

Here, we performed a systematic integrative analysis combining bulk transcriptomics (CGGA, 693 expression profiles; 692 samples with WHO-grade labels), WGCNA, systematic machine-learning screening (8 algorithms with cross-validation), immune infiltration profiling, scRNA-seq validation (54,978 cells), virtual knockout analysis, LASSO-Cox prognostic modeling, and Scissor-guided phenotype–cell mapping to identify ferroptosis-related grade-discriminative and prognostic biomarkers for glioma.

2. Materials and Methods

2.1. Data Acquisition and Processing

The CGGA mRNAseq_693 dataset (RSEM-normalized) was obtained from the Chinese Glioma Genome Atlas (CGGA; http://www.cgga.org.cn). It contained 693 expression profiles. Of these, 692 had interpretable WHO-grade annotations: 249 GBM (WHO grade IV) and 443 LGG (WHO grade II-III). The remaining sample, CGGA_D49, lacked

grade, histology, and survival annotations and was excluded from all grade-dependent and survival analyses but retained for unsupervised WGCNA. Expression data were log2(TPM + 1)-transformed prior to analysis. For reproducible internal diagnostic evaluation, the 692 grade-labeled samples were partitioned after panel selection using class-stratified 70/30 sampling with random seed 42, yielding 486 training samples (175 GBM, 311 LGG) and 206 testing samples (74 GBM, 132 LGG). The prognostic analysis separately used 657 samples with complete survival data (460 training, 197 testing; 394 events). Independent external validation used GSE16011 (Gravendeel et al., 2009 [24]): 268 glioma samples had interpretable WHO-grade annotations (159 GBM and 109 LGG) for classification, and 224 had complete survival information (205 events) for prognostic validation. The complete cohort allocation and analysis flow is summarized in Figure S1.

2.2. Ferroptosis Gene Set

A comprehensive set of 263 ferroptosis-related genes was compiled from the FerrDb V2 database [25] and the literature, encompassing known ferroptosis drivers, suppressors, and markers.

2.3. Differential Expression Analysis

Differentially expressed genes (DEGs) between GBM and LGG were identified using the limma package [26] in R (v4.6.0). Significance thresholds were set at $|\log_2 FC| > 0.5$ and adjusted p-value < 0.05 (Benjamini–Hochberg). Volcano plots were generated using ggplot2.

2.4. Weighted Gene Co-Expression Network Analysis

WGCNA [27] was applied to the CGGA expression matrix using DEGs and ferroptosis genes as input (n = 3011 genes). A signed network was constructed with the selected soft-thresholding power (β = 5). Module ferroptosis gene enrichment was assessed using the hypergeometric test, and modules with adjusted $p < 0.05$ were considered ferroptosis-enriched.

2.5. Machine Learning Classification Model Construction

Eight machine-learning algorithms were systematically evaluated: ElasticNet, Random Forest, Ridge regression, SVM-radial, LASSO, SVM-linear, GBM, and KNN. Five-fold cross-validation with class-balanced sampling was used for screening, and performance was assessed by ROC-AUC. WGCNA used all 693 expression profiles, whereas grade-dependent differential expression and machine-learning screening used the 692 samples with WHO-grade labels. These upstream discovery steps preceded the diagnostic split. After the 12-gene panel was fixed, a standardized ElasticNet logistic model restricted to these genes was fitted using only the 486-sample training set. Missing predictor values, scaling parameters, regularization strength, and all model coefficients were estimated without access to test outcomes. Hyperparameter selection used five-fold cross-validation within the training set (elastic-net mixing parameter 0.5). The model was applied unchanged to the 206-sample test set. Because test samples contributed to upstream WGCNA and feature discovery, the test set is not fully independent and its AUC may remain optimistic. A fully nested workflow repeating all discovery steps within each outer training fold would be required for an internally unbiased estimate; such a nested re-analysis was not performed. The exact allocation is supplied and summarized in Figure S1.

2.6. Immune Infiltration Analysis

Immune cell abundance was estimated using ssGSEA with 18 cell-type-specific gene signatures (B cells, CD4+ T cells, CD8+ T cells, Tregs, NK cells, monocytes, M0/M1/M2 macrophages, dendritic cells, neutrophils, mast cells, eosinophils, plasma cells, gamma-

delta T cells). Differentially infiltrating immune cell types between GBM and LGG were identified by the Wilcoxon rank-sum test. Spearman correlations between core biomarker expression and immune cell scores were calculated.

2.7. Single-Cell RNA-seq Data Processing and Validation Strategy

scRNA-seq data from 54,978 cells across 19 glioma patients (GSE247824, GSE159416) were obtained from GEO. These data were used (i) to confirm that the core biomarkers are expressed in defined glioma cell populations, and (ii) as the input for the virtual knockout analysis, following the rationale that single-cell transcriptomes capture cell-state-specific regulatory wiring that bulk data cannot resolve [19,20]. Data were processed using Seurat v5 [28].

2.8. Virtual Knockout Method

To predict the functional impact of core ferroptosis biomarker perturbation, we used the scTenifoldKnk algorithm [21], which constructs gene regulatory networks (GRNs) from single-cell expression data via tensor decomposition of multiple PC-regression networks, simulates the knockout of a target gene by removing its regulatory edges, and quantifies the resulting differential regulation of all other genes using a Z-score statistic with Benjamini–Hochberg correction. Briefly, for each target gene, 10 networks were constructed from 500-cell subsamples of the scRNA-seq count matrix (n = 1505 highly variable genes), combined via tensor decomposition, and the knockout network was compared with the wild-type network through manifold alignment. Genes with adjusted $p < 0.05$ were considered significantly perturbed. Virtual knockout provides computational predictions that require experimental validation and are interpreted accordingly.

2.9. Prognostic Risk Score Model Construction and Evaluation

To extend the 12-gene panel to prognostic prediction, the risk score was constructed using LASSO-penalized Cox regression (glmnet package, alpha = 1) with 10-fold cross-validation in the CGGA cohort (n = 657 with survival data; model fitting and cutoff optimization were performed on this cohort). The performance of the fitted model was then evaluated in the held-out prognostic test set (n = 197) of the 70/30 stratified split (see Section 2.1). Both the minimum partial-likelihood deviance (λ_min) and the 1-standard-error criterion (λ_1se) were evaluated. Patients were stratified into high- and low-risk groups using the optimal cutoff determined by surv_cutpoint (survminer package). Kaplan–Meier survival curves with log-rank tests and time-dependent receiver operating characteristic (ROC) curves were used to evaluate prognostic performance. Multivariate Cox regression was performed to assess the independent prognostic value of the risk score adjusting for age and WHO grade. A nomogram was constructed using the rms package for individualized survival prediction, with calibration curves to evaluate predictive accuracy.

2.10. Scissor-Guided Phenotype–Cell Mapping Method

To identify cell subpopulations associated with clinical outcomes, the Scissor algorithm was applied to integrate CGGA bulk transcriptomic data (n = 657) with scRNA-seq profiles (n = 10,000 randomly sampled cells). The Pearson correlation matrix between single cells and bulk samples was used as input to an elastic-net regression model with the Cox family (alpha = 0.05, cutoff = 0.25). Cells were classified as Scissor+ (positively associated with poor survival), Scissor− (associated with favorable survival), or background. The distribution of Scissor-labeled cells across transcriptional clusters was visualized on the UMAP embedding and quantified by proportion analysis.

2.11. Statistical Analysis

All statistical analyses were performed in R v4.6.0. Group comparisons used Wilcoxon rank-sum tests unless otherwise specified. Multiple testing correction employed the Benjamini–Hochberg method. Correlation analyses used Spearman's rank correlation coefficient.

3. Results

3.1. Ferroptosis Gene Expression Landscape in Glioma

The gene-screening cascade is summarized in Figure 1. To characterize ferroptosis gene-expression dysregulation in glioma, we analyzed the 692 CGGA samples with WHO-grade labels (249 GBM and 443 LGG). Limma differential expression analysis identified 2798 DEGs between GBM and LGG ($|\log2FC| > 0.5$, adjusted $p < 0.05$), of which 50 were ferroptosis-related genes (Figure 2). Among the panel genes, TFRC showed directionally higher expression in GBM (log2FC = +0.40, adjusted $p = 6.0 \times 10^{-7}$), whereas GCLC (log2FC = −0.43), SLC7A11 (−0.20), and ALOX15 (−0.05) were more highly expressed in LGG. Individual panel genes did not all exceed the $|\log2FC| > 0.5$ threshold; the 12-gene panel was selected by machine learning from the 76 WGCNA-enriched genes (Section 3.3), with DEG analysis serving as an independent landscape characterization rather than a filtering step.

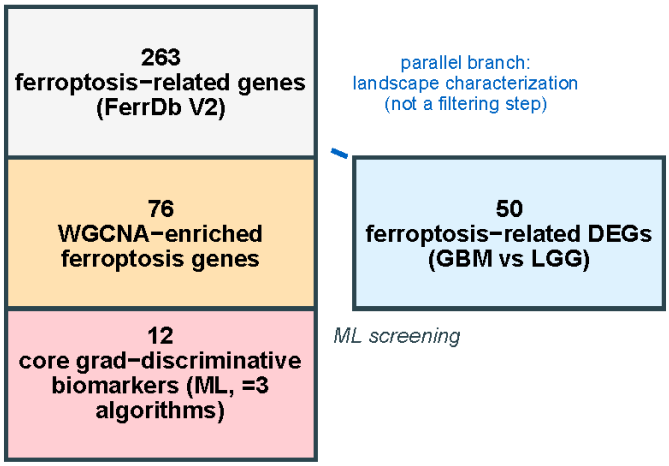


Figure 1. Gene screening cascade. Bar chart showing the sequential filtering of candidate genes: 263 ferroptosis-related genes from FerrDb V2 → 76 WGCNA-enriched module genes (ferroptosis-enriched modules, hypergeometric $p < 0.05$) → 12 core grade-discriminative biomarkers selected by ≥3 of 8 machine learning algorithms with 5-fold cross-validation (ML screening). The 50 ferroptosis-related DEGs between GBM and LGG (limma, $|\log_2FC| > 0.5$, BH-adjusted $p < 0.05$) are shown as a parallel branch of the landscape characterization (Figure 2) and were not a filtering step in the panel pipeline.

3.2. WGCNA Identifies a Ferroptosis-Enriched Module

WGCNA was applied to 3011 genes (DEGs + ferroptosis genes) in the CGGA cohort. The signed network, constructed with soft-thresholding power β = 5, identified 8 distinct co-expression modules (Figure 1). Module ferroptosis gene enrichment analysis revealed that module 6 (red) was highly significantly enriched for ferroptosis genes: 66 of 81 module genes were ferroptosis-related (hypergeometric test $p = 5.8 \times 10^{-61}$, enrichment ratio = 10.27). An additional module (module 0, grey) containing 25 genes with 10 ferroptosis genes also showed significant enrichment (adjusted $p = 3.7 \times 10^{-5}$). A total of 76 unique ferroptosis-related genes derived from these enriched modules were carried forward for machine learning analysis.

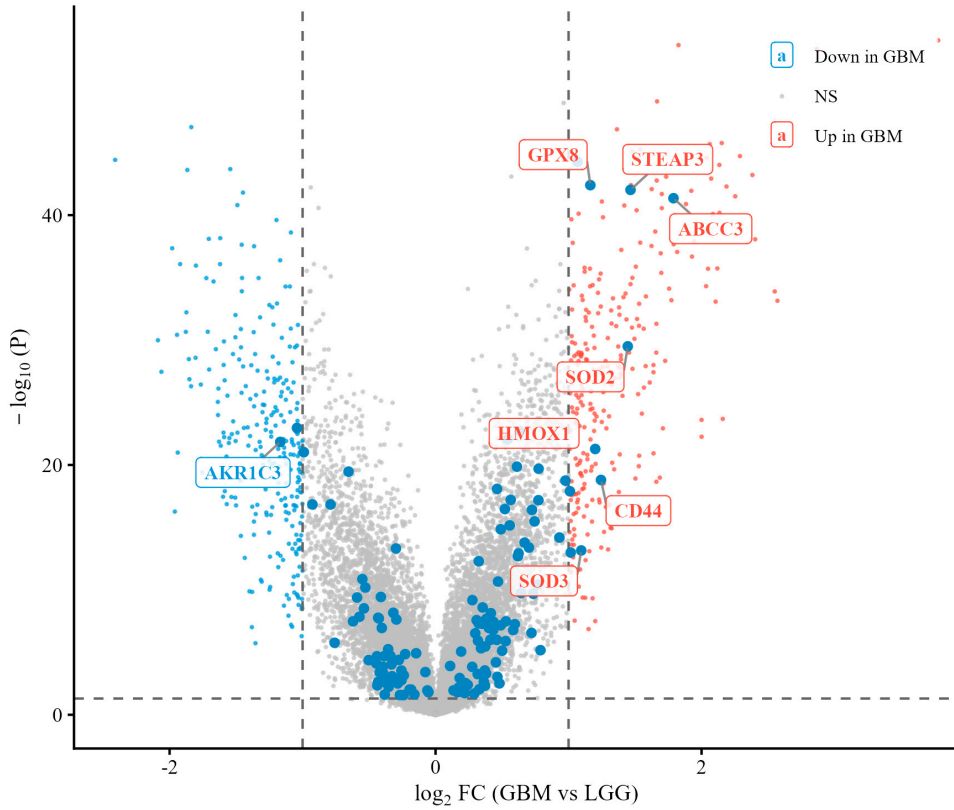


Figure 2. Differential expression landscape. Volcano plot of 2798 differentially expressed genes between GBM (n = 249) and LGG (n = 443) in the CGGA cohort (limma, $|\log_2 FC| > 0.5$, BH-adjusted $p < 0.05$). Red: upregulated in GBM; blue: downregulated in GBM; orange: significant at adjusted $p < 0.05$ only; grey: not significant. Ferroptosis-related genes are highlighted as labeled points.

3.3. Machine Learning Screening Identifies 12 Core Grade-Discriminative Biomarkers

Using the 76 WGCNA-derived ferroptosis genes as features, we systematically evaluated 8 machine-learning algorithms with 5-fold cross-validation. ElasticNet achieved the numerically highest cross-validation AUC (0.8523), closely followed by Random Forest (0.8522), Ridge (0.8518), and SVM-radial (0.8494), all within a narrow range of 0.003 AUC (Figure 3a). We therefore do not interpret ElasticNet as statistically superior to Random Forest or Ridge. ElasticNet was selected as the reference model because it combined the numerically highest AUC with regularization, coefficient-based interpretability, and a compact implementation suitable for a fixed multigene panel. The comparable performance of regularized linear and tree-based models supports the presence of a reproducible multigene signal rather than a model-specific advantage. LASSO (0.8453) and SVM-linear (0.8402) were also competitive, whereas GBM (0.8308) and KNN (0.7943) performed less well.

Feature importance analysis across all models identified 12 genes selected by $\geq$3 models as core grade-discriminative biomarkers (Figure 3b, Table 1): ALOX15, TFRC, GCLC, DPP8, MBOAT2, NCOA4, NOX5, PIK3CB, CISD2, AMD1, TFR2, and TRAF6. Among these, ALOX15 was the top feature in ElasticNet and LASSO and received the highest importance weight in ElasticNet (normalized importance = 100). TFRC was the top feature in Random Forest and GBM, suggesting complementary feature selection across algorithms.

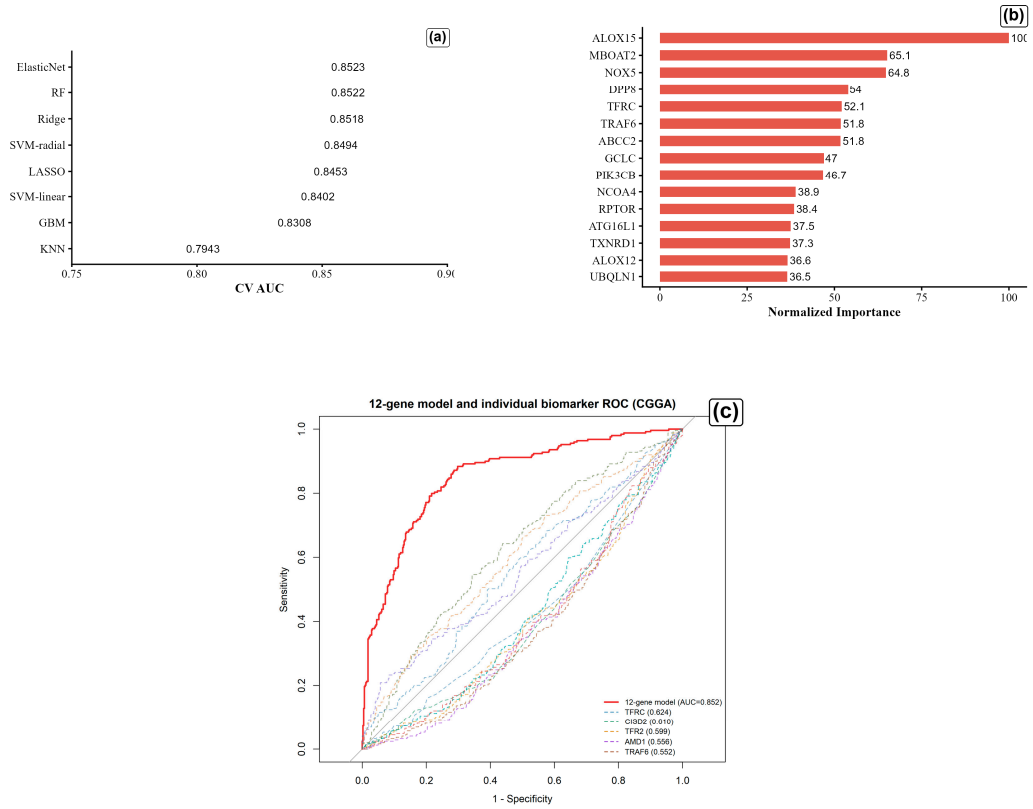


Figure 3. Machine-learning screening and feature selection. (**a**) Screening-stage cross-validation AUC of 8 algorithms (5-fold, class-balanced; 692 grade-labeled CGGA samples): ElasticNet 0.8523, Random Forest 0.8522, Ridge 0.8518, SVM-radial 0.8494, LASSO 0.8453, SVM-linear 0.8402, GBM 0.8308, and KNN 0.7943. (**b**) Top 15 features ranked by normalized ElasticNet importance (ALOX15 = 100); core biomarkers are highlighted. (**c**) In-sample screening-stage ROC curves for ElasticNet and representative individual biomarkers. The independent internal test result for the fixed 12-gene model is shown in Figure S5a.

The screening-stage ElasticNet analysis achieved a five-fold cross-validation AUC of 0.852. Its corresponding in-sample operating characteristics were ROC-AUC 0.852 (95% CI 0.822–0.882), average precision 0.771, sensitivity 0.614, specificity 0.874, precision 0.732, and F1 score 0.668 at a 0.5 threshold. Per-gene univariate analysis showed modest discrimination (TFRC AUC = 0.624, CISD2 = 0.610, TFR2 = 0.599), supporting the multigene combination (Figure S2). After the panel was fixed, the 692 grade-labeled samples were reproducibly divided using class-stratified sampling (seed 42) into training (n = 486; 175 GBM and 311 LGG) and testing (n = 206; 74 GBM and 132 LGG) sets. A standardized 12-gene ElasticNet model was fitted and tuned only within the training set and applied unchanged to the test set, yielding an AUC of 0.847 (bootstrap 95% CI 0.790–0.896; Figure S5a). Because WGCNA and feature selection preceded this split, this remains an internal evaluation with potential optimism rather than a fully independent estimate. Independent GSE16011 validation used all 268 grade-annotated samples (159 GBM and 109 LGG) and the 10 cross-platform-mapped genes (NOX5 and CISD2 were excluded specifically because reliable GPL8542 microarray probes could not be mapped), yielding an AUC of 0.775 (95% CI 0.718–0.832; Figure S5b). As an orthogonal directional check, four iron-metabolism genes (TFRC, TFR2, TRAF6, and NCOA4) showed a normal brain < LGG < GBM expression gradient in GSE16011 (Figure S3).

Table 1. Twelve core ferroptosis-related grade-discriminative biomarkers identified by systematic machine learning screening.

Gene	Full Name	Normalized ElasticNet Importance	Top Model(s)
ALOX15	Arachidonate 15-lipoxygenase	100.00	ElasticNet, LASSO, Ridge
MBOAT2	Membrane-bound O-acyltransferase domain containing 2	65.14	ElasticNet
NOX5	NADPH oxidase 5	64.76	ElasticNet
DPP8	Dipeptidyl peptidase 8	53.96	ElasticNet
TFRC	Transferrin receptor	52.06	Random Forest, GBM
TRAF6	TNF receptor-associated factor 6	51.84	ElasticNet
GCLC	Glutamate–cysteine ligase catalytic subunit	47.05	SVM-radial, SVM-linear, KNN
PIK3CB	Phosphatidylinositol-4,5-bisphosphate 3-kinase catalytic subunit beta	46.73	ElasticNet
NCOA4	Nuclear receptor coactivator 4	38.90	ElasticNet
CISD2	CDGSH iron sulfur domain 2	4.59	Multiple
AMD1	Adenosylmethionine decarboxylase 1	33.00	Multiple
TFR2	Transferrin receptor 2	28.04	Multiple

Note: All 12 genes were selected by at least 3 of 8 machine-learning algorithms during screening of the 692 grade-labeled CGGA samples. The reported screening-stage ElasticNet cross-validation AUC was 0.852. Normalized importance is relative to ALOX15 = 100.

3.4. Immune Microenvironment Dysregulation in GBM

Immune infiltration analysis using ssGSEA revealed striking differences between GBM and LGG (Table 2). GBM showed significantly elevated levels of plasma cells (GBM 2.67 vs. LGG 2.09, $p < 0.001$), M2 macrophages (1.34 vs. 0.83, $p < 0.001$), CD8+ T cells (1.17 vs. 0.72, $p < 0.001$), and monocytes (6.23 vs. 5.44, $p < 0.001$). In contrast, B cell memory scores were significantly lower in GBM (1.36 vs. 1.60, $p < 0.001$), suggesting an imbalance between adaptive and innate immunity.

Table 2. Immune cell infiltration differences between GBM and LGG assessed by ssGSEA.

Immune Cell Type	Mean GBM	Mean LGG	Δ (GBM − LGG)	*p*-Value	*p*-Adjusted
Plasma cells	2.67	2.09	0.58	$<10^{-15}$	$<10^{-15}$
Macrophages: M2	1.34	0.83	0.51	$<10^{-15}$	$<10^{-15}$
T cells: CD8	1.17	0.72	0.45	$<10^{-15}$	$<10^{-15}$
Monocytes	6.23	5.44	0.79	6.7×10^{-16}	3.0×10^{-15}
Macrophages: M0	4.66	3.77	0.88	2.0×10^{-14}	7.4×10^{-14}
T cells: CD4-naïve	2.13	1.83	0.30	1.3×10^{-11}	4.0×10^{-11}
T cells: regulatory (Tregs)	0.49	0.31	0.19	1.3×10^{-10}	3.4×10^{-10}
T cells: CD4 memory	1.67	1.40	0.27	3.8×10^{-10}	8.5×10^{-10}
Eosinophils	0.28	0.17	0.11	4.6×10^{-9}	9.2×10^{-9}
Macrophages: M1	1.31	1.02	0.29	8.5×10^{-9}	1.5×10^{-8}
T cells: gamma delta	0.76	0.52	0.24	2.5×10^{-6}	4.1×10^{-6}
B cells: memory	1.36	1.60	−0.24	7.0×10^{-6}	1.1×10^{-5}
B cells: naïve	0.63	0.53	0.10	1.3×10^{-5}	1.8×10^{-5}
Neutrophils	1.38	1.17	0.21	3.1×10^{-5}	4.0×10^{-5}
Dendritic cells	2.45	2.40	0.06	0.166	0.200
Mast cells	0.93	0.90	0.03	0.611	0.686
T cells: follicular	2.04	2.04	<0.01	0.674	0.686
NK cells	1.69	1.66	0.03	0.686	0.686

Note: *p*-values from Wilcoxon rank-sum test; *p*-adjusted by Benjamini–Hochberg correction. GBM $n = 249$, LGG $n = 443$, CGGA cohort.

Correlation analysis between core ferroptosis biomarkers and immune cell types revealed a broad positive association with dendritic cells and CD4+ T cells (Figure 4). AMD1 showed the strongest overall correlation with dendritic cells ($\rho = 0.607$, $p = 6.3 \times 10^{-71}$), followed by TRAF6 ($\rho = 0.550$, $p = 5.5 \times 10^{-56}$). PIK3CB ($\rho = 0.495$, $p = 3.6 \times 10^{-44}$), NCOA4 ($\rho = 0.494$, $p = 6.6 \times 10^{-44}$), and TFRC ($\rho = 0.440$, $p = 3.6 \times 10^{-34}$) also showed robust dendritic cell associations. Intriguingly, MBOAT2 was negatively correlated with NK cells ($\rho = -0.366$, $p = 2.4 \times 10^{-23}$), suggesting a potential immunosuppressive function. Representative expression distributions of the panel genes are shown in Figure 5.

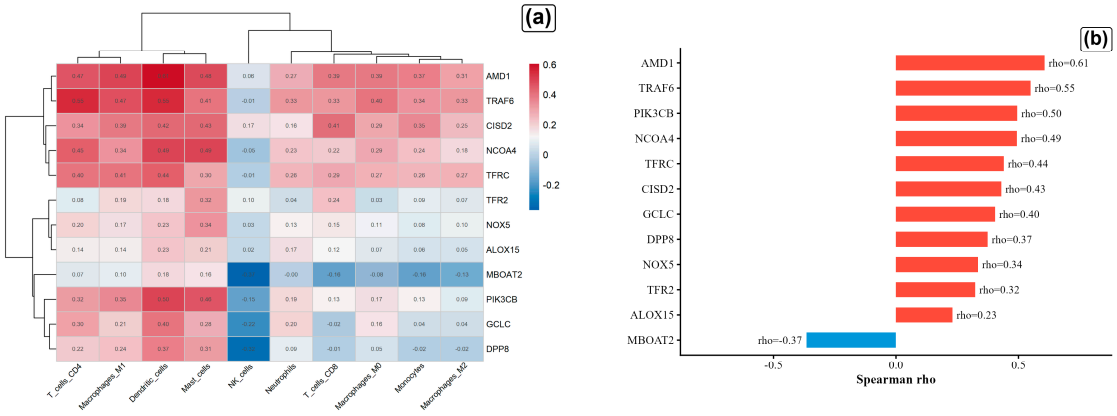


Figure 4. Immune microenvironment analysis. (**a**) Heatmap of Spearman correlations between 12 core biomarkers and 18 immune cell types (ssGSEA scores; CGGA, $n = 693$). Red: positive correlation; blue: negative. (**b**) Bar chart of the strongest immune correlation for each core biomarker. GBM showed significantly elevated plasma cells, M2 macrophages, CD8+ T cells, and monocytes (Wilcoxon rank-sum test, BH-adjusted $p < 0.001$; Table 2).

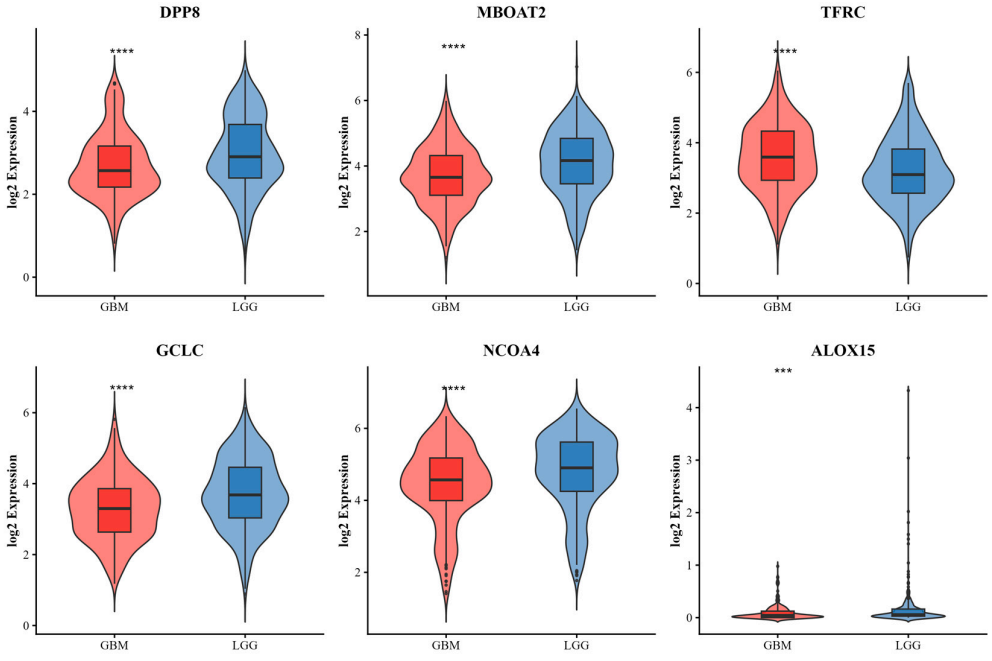


Figure 5. Core biomarker expression in GBM vs. LGG. Violin plots of six representative panel genes (AMD1, MBOAT2, TFRC, GCLC, NCOA4, and ALOX15) comparing expression between GBM ($n = 249$) and LGG ($n = 443$) in the CGGA cohort (log2(TPM+1) scale). Asterisks denote Wilcoxon rank-sum test significance: *** $p < 0.001$; **** $p < 0.0001$. Expression results for all 12 panel genes are provided in Table 1.

3.5. Single-Cell RNA-seq Validation Results

To validate biomarker expression at single-cell resolution, we analyzed an integrated scRNA-seq dataset of 54,978 cells from 19 glioma patients (GSE247824, GSE159416). Unsupervised clustering resolved 45 transcriptionally distinct clusters (resolution 0.5), which were assigned to 12 annotation labels, which were consolidated into 11 major cell categories by reporting TAM_Macrophage and TAM_Microglia jointly as TAMs based on canonical marker gene expression: tumor-associated macrophages (TAMs, 23,839 cells; 43.4%, comprising TAM_Macrophage and TAM_Microglia subsets), NK cells (10,210), T cells (7015), neutrophils (5288), malignant cells (2775), fibroblasts (2515), B cells (1687), oligodendrocytes (1318), endothelial cells (70), astrocytes (67), and pericytes (194). Eleven of the 12 core biomarkers were represented in the integrated single-cell expression matrix; NOX5 was not available in this single-cell dataset, whereas TFR2 was retained. FeaturePlot visualization revealed that ALOX15, TFRC, GCLC, and TRAF6 showed broad expression across multiple cell populations, with highest overall expression in TAMs and malignant cells. DPP8, CISD2, and AMD1 were more uniformly expressed. Ferroptosis module score analysis confirmed elevated ferroptosis activity in IDH-wildtype compared to IDH-mutant tumors ($p < 0.001$, Wilcoxon test), consistent with the known aggressiveness of IDHwt gliomas (Figure S4). Subset analysis of TAMs ($n = 23{,}839$ cells) confirmed ferroptosis gene expression across TAM subclusters, with particularly high ALOX15 and TFRC expression in the TAM_Macrophage subset relative to TAM_Microglia (Figure S6).

3.6. Virtual Knockout Results

To explore the predicted regulatory consequences of core-biomarker perturbation, we applied the scTenifoldKnk virtual-knockout algorithm to the scRNA-seq data (Figure 6, Table 3). Virtual knockout of TFRC, GCLC, and TRAF6—genes related to iron uptake, glutathione synthesis, and inflammatory signaling, respectively—was predicted to perturb a shared set of 27 genes associated with neural development and glioma stemness, including SOX2, NES, PTPRZ1, TCF4, MAP1B, QKI, GNAS, and CDK6 (adjusted $p < 10^{-5}$) (Table 3). This computational convergence suggests a testable relationship between these ferroptosis-related inputs and a stemness-associated transcriptional program; it does not demonstrate a causal mechanism. ALOX15 virtual knockout uniquely predicted perturbation of genes involved in polyamine metabolism (OAZ1, adjusted $p = 5.2 \times 10^{-85}$), mitochondrial ATP synthase (ATP5MC2), vesicular trafficking (VAMP8), and ribosomal biology (RPL7 and RPS23), whereas NCOA4 virtual knockout produced no statistically significant downstream predictions.

To obtain orthogonal evidence from an independent public resource, we reanalyzed DepMap CRISPR-Cas9 gene-effect data (Project Achilles, 22Q2) from 67 glioma cell lines. NCOA4 showed a dependency signal in 33/67 lines (49%; mean CERES = −0.563), and TFRC in 16/67 lines (24%; mean CERES = −0.402) (Figure 6b, Table 4). AMD1 (mean CERES = −0.363) and PIK3CB (−0.210) showed weaker dependency signals, whereas ALOX15, GCLC, TFR2, MBOAT2, DPP8, TRAF6, NOX5, and CISD2 were non-essential on average (mean > −0.2). RPS23 and RPL7, which were predicted as ALOX15 downstream targets, were strongly dependent across the 67 lines; however, because ribosomal proteins are broadly pan-essential, this observation does not constitute ALOX15-specific validation. Thus, the DepMap analysis provides partial, orthogonal public-screen corroboration for the biological relevance of TFRC and NCOA4 but is not a new functional experiment and does not experimentally validate the scTenifoldKnk mechanism. The virtual-knockout results remain hypothesis-generating predictions for future targeted perturbation studies.

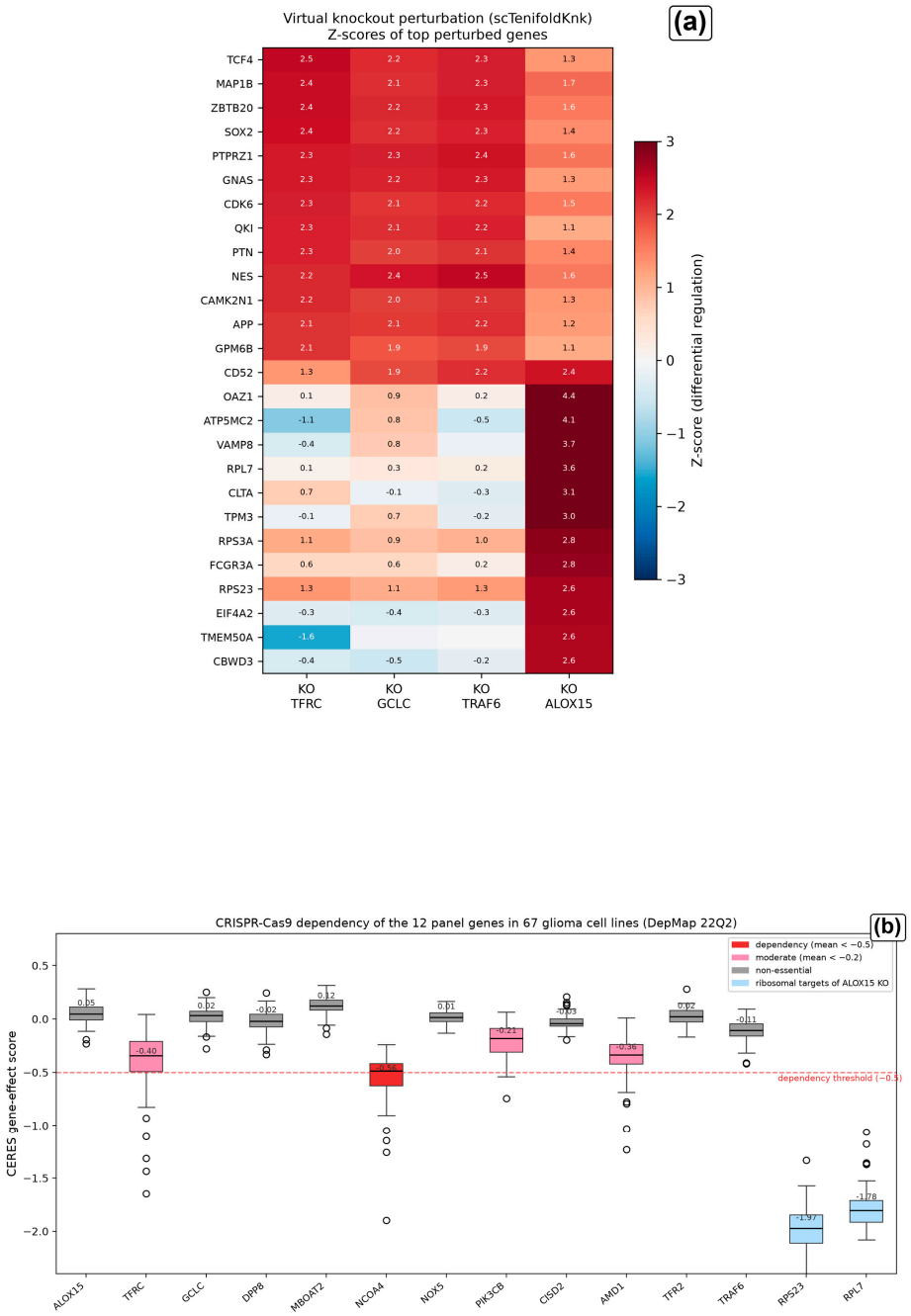


Figure 6. Virtual knockout and CRISPR-Cas9 dependency validation. (**a**) Heatmap of scTenifoldKnk differential-regulation Z-scores for the top perturbed genes following virtual knockout of TFRC, GCLC, TRAF6, and ALOX15 (scRNA-seq, 1505 highly variable genes; networks built from 500-cell subsamples, 10 networks per target gene; red = up-regulated regulatory effect; blue = down-regulated). TFRC/GCLC/TRAF6 knockouts converge on a stemness-associated program (SOX2, NES, PTPRZ1, TCF4, MAP1B, QKI, GNAS, CDK6); ALOX15 knockout uniquely perturbs OAZ1, ATP5MC2, VAMP8, RPL7, RPS23. NCOA4 knockout produced no significant perturbation. (**b**) Box plots of CERES gene-effect scores for the 12 panel genes across 67 glioma cell lines (DepMap 22Q2), with the ribosomal genes RPS23 and RPL7 shown as references. Dashed line at −0.5 marks the dependency threshold. NCOA4 (mean −0.563; 49% dependent lines) and TFRC (mean −0.402; 24%) are dependency genes; ALOX15 (mean +0.047) is non-essential. Red boxes: dependency; pink: moderate; grey: non-essential; blue: ribosomal reference (pan-essential).

Table 3. Top perturbed genes predicted by scTenifoldKnk virtual knockout.

Knockout	Top Perturbed Genes (*p*.adj < 0.05)
tfrc (*n* = 31)	TCF4, MAP1B, ZBTB20, SOX2, PTPRZ1, GNAS, CDK6, QKI, PTN, NES
GCLC (*n* = 43)	NES, PTPRZ1, GNAS, ZBTB20, TCF4, SOX2, QKI, MAP1B, CDK6, APP
TRAF6 (*n* = 39)	NES, PTPRZ1, GNAS, ZBTB20, TCF4, MAP1B, SOX2, QKI, CDK6, APP
ALOX15 (*n* = 17)	OAZ1, ATP5MC2, VAMP8, RPL7, CLTA, TPM3, RPS3A, FCGR3A, RPS23, EIF4A2
NCOA4 (*n* = 0)	— (no significant perturbation)

Table 4. CRISPR-Cas9 dependency signals for core biomarkers in 67 glioma cell lines (DepMap 22Q2).

Gene	Mean CERES	Dependency Lines (*n*)	Dependency (%)
NCOA4	−0.563	33	49%
TFRC	−0.402	16	24%
AMD1	−0.363	10	15%
PIK3CB	−0.210	3	4%
TRAF6	−0.110	0	0%
DPP8	−0.017	0	0%
GCLC	+0.021	0	0%
TFR2	+0.022	0	0%
ALOX15	+0.047	0	0%
MBOAT2	+0.116	0	0%
NOX5	+0.014	0	0%
CISD2	−0.032	0	0%

Note: CERES gene-effect scores from DepMap 22Q2 (Project Achilles); a score < −0.5 indicates dependency (knockout inhibits proliferation). All 12 panel genes were covered by the CRISPR panel; NOX5 (mean CERES +0.014) and CISD2 (−0.032) showed no functional dependency.

3.7. Scissor-Guided Phenotype–Cell Mapping Results

To identify cell subpopulations associated with clinical outcomes, we applied the Scissor algorithm to integrate CGGA bulk survival data (*n* = 657) with scRNA-seq profiles (10,000 sampled cells). Using elastic-net regularization (alpha = 0.05, cutoff = 0.25), we identified 43 Scissor+ cells (positively associated with poor survival) and 14 Scissor− cells (associated with favorable survival). The Scissor+ cells were non-randomly distributed across transcriptional clusters (Figure 7e), predominantly enriched in specific clusters (Figure 7f). Differential expression analysis between Scissor− and background cells identified 21 significantly dysregulated genes (*p*_adj < 0.05), with enrichment in immune-related pathways (Figure S4).

3.8. Prognostic Risk Score Model Performance

To extend the 12-gene panel to prognostic stratification, we constructed a risk score model using LASSO-Cox regression in the CGGA cohort (*n* = 657 with survival data; 394 events). All 12 core biomarkers were retained at the optimal regularization parameter (λ_min = 0.0055) (Table 5). TRAF6 showed the strongest risk-associated coefficient (HR = 2.60), while DPP8 showed the strongest protective effect (HR = 0.66). Patients were stratified into high-risk (*n* = 315) and low-risk (*n* = 342) groups using the surv_cutpoint-optimized threshold (Figure 7a). Kaplan–Meier analysis revealed significantly worse overall survival in the high-risk group (HR = 3.75, 95% CI 3.04–4.62, log-rank $p < 0.0001$; reference: low-risk group). Time-dependent ROC analysis demonstrated robust predictive accuracy, with AUC values of 0.741 (1-year), 0.791 (2-year), 0.763 (3-year), and 0.768 (5-year) (Figure 7b).

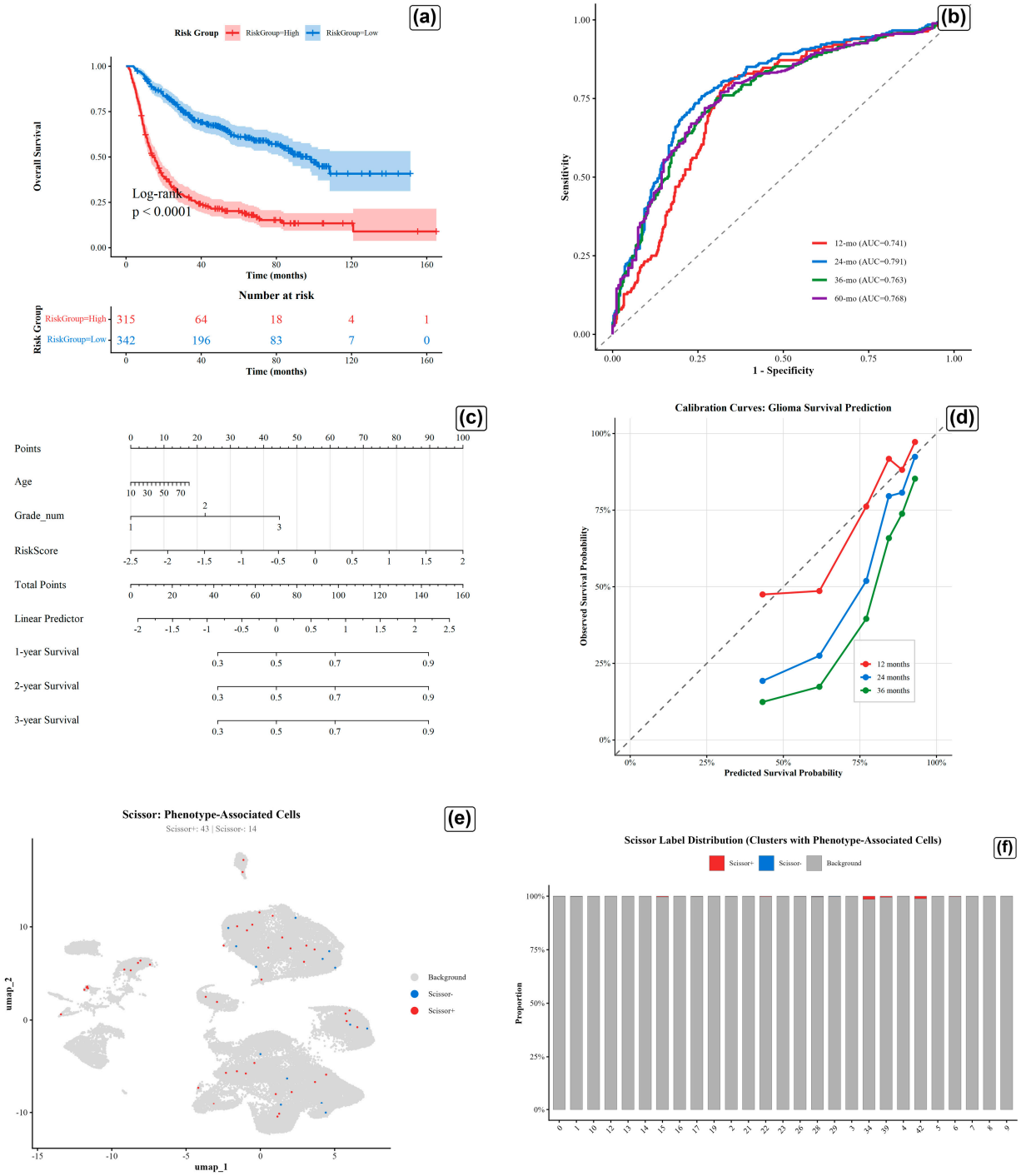


Figure 7. Prognostic risk score model and Scissor mapping. (**a**) Kaplan–Meier curves of overall survival for high-risk (n = 315) vs. low-risk (n = 342) groups in CGGA (log-rank $p < 0.0001$; HR = 3.75, 95% CI 3.04–4.62; risk score = LASSO-Cox 12-gene linear predictor). (**b**) Time-dependent ROC curves for the risk score at 1, 2, 3, and 5 years (AUC 0.741, 0.791, 0.763, 0.768). (**c**) Nomogram integrating age, WHO grade, and risk score for 1-, 2-, and 3-year survival prediction. (**d**) Calibration curves for the nomogram (1-year MAE = 0.051). (**e**) UMAP projection of scRNA-seq cells colored by Scissor classification (43 Scissor+, 14 Scissor−, background; 10,000 cells analyzed); (**f**) distribution of Scissor labels across cell clusters.

Table 5. LASSO-Cox regression coefficients for the 12-gene prognostic risk score model.

Gene	Coefficient	Hazard Ratio (HR)	Direction
TRAF6	0.956	2.60	Risk
AMD1	0.350	1.42	Risk
TFRC	0.316	1.37	Risk
ALOX15	0.192	1.21	Risk
TFR2	0.074	1.08	Risk
CISD2	−0.202	0.82	Protective
PIK3CB	−0.265	0.77	Protective
NCOA4	−0.340	0.71	Protective
DPP8	−0.420	0.66	Protective
MBOAT2	−0.097	0.91	Protective
NOX5	−0.050	0.95	Protective
GCLC	−0.023	0.98	Protective

Note: Coefficients from LASSO-Cox regression at λ_min = 0.0055 (10-fold cross-validation). HR > 1 indicates association with shorter survival (risk); HR < 1 indicates association with longer survival (protective). CGGA cohort, n = 657.

Multivariate Cox regression incorporating Age, WHO Grade, and the risk score confirmed the independent prognostic value of the risk score (HR = 2.02, 95% CI: 1.68–2.42, $p = 3.4 \times 10^{-14}$) (Table 6), comparable in effect size to WHO Grade III (HR = 2.43, $p = 6.3 \times 10^{-8}$) and WHO Grade IV (HR = 4.05, $p = 6.7 \times 10^{-15}$). A nomogram integrating these three variables was constructed for 1-, 2-, and 3-year survival prediction (Figure 7c) and calibration curves demonstrated good agreement between predicted and observed outcomes at 12 months (mean absolute error, MAE = 0.051). The calibration deviations widened at longer follow-up (24-month MAE = 0.161; 36-month MAE = 0.257), consistent with the increasing uncertainty inherent in Cox proportional hazards extrapolation over longer time horizons. The independent prognostic value of the risk score was confirmed in the held-out test set (n = 197), with an HR of 3.95 (95% CI: 2.10–7.43, log-rank $p < 0.0001$) and time-dependent AUC values of 0.712 (1-year), 0.780 (2-year), and 0.767 (3-year) (Figure S5c).

Table 6. Multivariate Cox regression analysis of overall survival.

Variable	HR	95% CI	*p* Value
Age	1.01	1.00–1.02	0.050
WHO Grade III (vs. II)	2.43	1.76–3.36	<0.0001
WHO Grade IV (vs. II)	4.05	2.85–5.77	<0.0001
Risk Score	2.02	1.68–2.42	<0.0001

Note: Multivariate Cox proportional hazards model including Age, WHO Grade, and the LASSO-derived 12-gene risk score. CGGA cohort, n = 657, 394 events.

Independent external prognostic validation was performed in the GSE16011 cohort (n = 224, 205 events). Because reliable GPL8542 microarray probes could not be mapped for NOX5 and CISD2, a LASSO-Cox model was re-trained on CGGA with the 10 cross-platform-mapped core genes (TFRC, TFR2, ALOX15, GCLC, TRAF6, NCOA4, DPP8, MBOAT2, PIK3CB, AMD1) and applied to GSE16011; patients were stratified into high- and low-risk groups by cohort median cutoff. As a consistency check, the 10-gene model performed equivalently to the full 12-gene model in the CGGA training cohort (C-index 0.704 vs. 0.708; risk-score correlation r = 0.985), indicating that the two platform-missing genes contribute little to the signature. The risk score demonstrated significant prognostic stratification with the high-risk group showing significantly worse survival (HR = 2.08, 95% CI: 1.56–2.78, log-rank $p < 0.001$) and time-dependent AUC values of 0.661 (1-year), 0.705 (2-year), 0.748

(3-year), and 0.663 (5-year) (Figure S5d). These results validate the prognostic generalizability of the signature across independent cohorts and microarray platforms, with a hazard-ratio direction consistent with the training cohort.

3.9. Biomarker Interaction and Coordination

The virtual-knockout analysis predicted that TFRC, GCLC, and TRAF6 perturbations converge on a shared stemness-associated transcriptional program (27 commonly perturbed genes, Figure 6), whereas reanalysis of public DepMap data showed dependency signals for the iron-metabolism genes NCOA4 and TFRC in subsets of glioma cell lines (Table 4). Together, these computational results suggest a putative relationship between ferroptosis-related expression features, iron metabolism, and the malignant stemness state. They should be considered hypothesis-generating rather than evidence of a demonstrated mechanistic axis.

4. Discussion

In this study, we performed a systematic integrative screening of ferroptosis-related grade-discriminative biomarkers for glioma through the successive application of DEG analysis, WGCNA, comprehensive machine learning evaluation (8 algorithms), immune infiltration profiling, single-cell transcriptomic validation, virtual knockout perturbation analysis, and reanalysis of public CRISPR-Cas9 dependency data. This multi-platform approach identified 12 core ferroptosis biomarkers with convergent computational and cross-platform support, of which the iron-metabolism genes NCOA4 and TFRC showed dependency signals in glioma cell lines.

4.1. ALOX15 as a Top-Ranked Grade-Discriminative Feature

Arachidonate 15-lipoxygenase (ALOX15) emerged as the top-ranked feature across ElasticNet, LASSO, and Ridge models. ALOX15 catalyzes the peroxidation of polyunsaturated fatty acids in cellular membranes, a committed step in ferroptosis [29]. In glioma, ALOX15 has been implicated in tumor progression and immune modulation, but its role as a grade-discriminative biomarker has received limited attention. Although the individual discriminative power of ALOX15 was modest in univariate analysis (AUC = 0.42), and ALOX15 was more highly expressed in LGG than in GBM ($\log_2$FC = -0.05, Figure 5), its importance within the multivariate ElasticNet model indicates that it contributes non-redundant information when combined with the other panel members, consistent with its function as a transcriptional marker of the ferroptosis-related state rather than a functional driver. Notably, both the virtual knockout analysis and the DepMap CRISPR screen indicated that ALOX15 is not a functional dependency in glioma cells (mean CERES +0.047), suggesting that ALOX15 functions primarily as a transcriptional marker of the ferroptosis-related state rather than an essential node, whereas the iron-metabolism genes within the same panel (NCOA4, TFRC) are functionally required.

4.2. Iron Metabolism and Ferritinophagy: TFRC and NCOA4

TFRC (transferrin receptor) was the second-ranked feature and was selected as the top predictor by both Random Forest and GBM models, and it showed the highest individual AUC (0.624) among the 12 panel genes. TFRC mediates cellular iron uptake, and its overexpression in glioma has been associated with poor prognosis [30]. Our findings extend this by demonstrating TFRC's grade-discriminative value in distinguishing GBM from LGG, consistent with the heightened iron demand of aggressive tumors. NCOA4, a selective cargo receptor for ferritinophagy (ferritin degradation by autophagy) [31], represents a mechanistically linked but distinct biomarker. NCOA4-mediated ferritin degradation releases free iron that can fuel Fenton chemistry and lipid peroxidation [32].

4.3. Glutathione Metabolism: GCLC as an Antioxidant Sentinel

GCLC (glutamate–cysteine ligase catalytic subunit) catalyzes the rate-limiting step in glutathione biosynthesis, and its expression directly determines cellular glutathione content and ferroptosis susceptibility [6]. GCLC was the top predictor in SVM models (both linear and radial) and the fourth-ranked overall. In the immune microenvironment, GCLC expression showed a strong positive correlation with dendritic cells ($\rho = 0.405$, $p = 1.2 \times 10^{-28}$), suggesting a potential link between glutathione metabolism and antigen-presenting cell function in the glioma TME. This aligns with recent evidence that glutathione levels regulate dendritic cell maturation and T-cell priming [33].

4.4. TRAF6: Bridging Inflammation and Ferroptosis

TRAF6 (TNF receptor-associated factor 6) is a critical adaptor protein for NF-κB and MAPK signaling downstream of Toll-like receptors and the IL-1 receptor [34]. The identification of TRAF6 as a core ferroptosis biomarker provides a molecular link between inflammatory signaling and ferroptosis susceptibility. In the prognostic model, TRAF6 carried the strongest risk-associated coefficient (HR = 2.60), and the strong TRAF6-dendritic cell correlation ($\rho = 0.550$) further implicates TRAF6 in immune–ferroptosis crosstalk.

4.5. Immune–Ferroptosis Crosstalk in the Glioma Microenvironment

Our immune infiltration analysis revealed a landscape of GBM-associated immune enrichment characterized by elevated plasma cells, M2 macrophages, and CD8+ T cells—consistent with the known immunosuppressive and inflamed phenotype of GBM [35,36]. The broad positive correlations between ferroptosis biomarkers and dendritic cells (AMD1 $\rho = 0.607$, TRAF6 $\rho = 0.550$, PIK3CB $\rho = 0.495$, all $p < 10^{-34}$) suggest that ferroptosis gene expression is linked to antigen-presenting cell infiltration in glioma. This association may reflect either ferroptosis-dependent DAMP release promoting dendritic cell recruitment [15] or the regulatory role of these genes beyond ferroptosis.

4.6. Comparison with Previous Ferroptosis Signatures

Several ferroptosis-related gene signatures have been reported for glioma prognosis, including the FRGPI (HMOX1, TFRC, JUN, SOCS1) [9] and 11-gene prognostic models [10]. Our 12-gene panel shows only partial overlap with these signatures (only TFRC is common), reflecting the distinct goal of grade discrimination versus prognostic stratification. The inclusion of DPP8, MBOAT2, NCOA4, NOX5, PIK3CB, CISD2, AMD1, TFR2, and TRAF6—not previously reported in glioma ferroptosis panels—represents a novel contribution. Among these, CISD2 (CDGSH iron sulfur domain 2) is of particular interest as it is an iron-sulfur cluster-containing protein implicated in mitochondrial iron homeostasis and has been linked to ferroptosis regulation, although its role in glioma has not been previously established. The systematic nature of our screening (8 algorithms, cross-validation, single-cell validation, virtual knockout) provides greater methodological rigor than prior studies that typically employed 1–3 machine learning methods.

4.7. Prognostic Value and Scissor-Guided Cell Mapping

Beyond grade discrimination, we demonstrated that the 12-gene panel carries significant prognostic information. The LASSO-Cox risk score achieved robust time-dependent AUC values (0.741–0.791) and stratified patients into groups with markedly different survival (HR = 3.75, $p < 0.0001$). Multivariate analysis confirmed the risk score as an independent prognostic factor (HR = 2.02, $p = 3.4 \times 10^{-14}$), with an effect size comparable to WHO grade. The external validation in GSE16011 ($n = 224$) confirmed both the direction and magnitude of the effect (HR = 2.08, $p < 0.001$). The prognostic value of

iron- and ferroptosis-related genes is consistent with previous findings [9,10]; however, our model is distinctive in being derived from a grade-discriminating gene panel rather than from purely prognostic screening, providing a unified framework. The calibration curves showed good 1-year accuracy (MAE = 0.051) but progressively wider deviations at 24 months (MAE = 0.161) and 36 months (MAE = 0.257), suggesting the risk score may be most reliable for shorter-term prognosis. The Scissor analysis, while identifying only a modest number of phenotype-associated cells (43 Scissor+ and 14 Scissor−), demonstrates the feasibility of linking bulk survival phenotypes with single-cell transcriptional states in glioma.

4.8. Limitations and Future Directions

This study has several limitations. First, CGGA provided 693 expression profiles, but only 692 had WHO-grade labels for grade-dependent analyses; the independent GSE16011 classification (n = 268, AUC = 0.775) and prognostic validation (n = 224, HR = 2.08) used distinct endpoint-specific subsets. Second, WGCNA and feature selection preceded the reproducible diagnostic split. Although the final 12-gene model was fitted and tuned using only the 486-sample training set and then applied unchanged to the 206-sample test set (AUC = 0.847, 95% CI 0.790–0.896), test samples contributed to upstream discovery, so this estimate may remain optimistic. The screening-stage AUC of 0.852 is likewise not an unbiased validation estimate for the final panel. We did not perform a fully nested re-analysis; repeating every discovery and modeling step within outer training folds would be required to eliminate this leakage. Third, virtual knockout is hypothesis-generating rather than demonstrative. DepMap provided partial functional corroboration, but the ALOX15 targets RPS23 and RPL7 are pan-essential and therefore do not provide gene-specific support. Fourth, scRNA-seq validation used one dataset and may not capture inter-patient heterogeneity. Fifth, batch effects between RNA-seq and microarray platforms cannot be completely eliminated despite within-cohort standardization. Prospective multi-center validation and mechanistic experiments remain necessary.

5. Conclusions

This study identifies and systematically evaluates a 12-gene ferroptosis panel that discriminates glioma grades and predicts survival through integrative machine learning, immune profiling, single-cell transcriptomics, virtual knockout perturbation analysis, and phenotype-guided cell mapping. Dependency signals for the iron-metabolism genes NCOA4 and TFRC in public glioma CRISPR-screen data provide partial orthogonal support for the biological relevance of the panel. The prognostic risk score and nomogram provide complementary tools for clinical risk stratification, while Scissor-based cell mapping links bulk survival phenotypes to transcriptional programs at single-cell resolution.

Supplementary Materials: The following supporting information can be downloaded at: https://www.mdpi.com/article/10.3390/biomedinformatics6050087/s1. Figure S1. Analysis workflow and sample accounting. WGCNA used all 693 CGGA expression profiles. Grade-dependent DEG and ML screening used 692 labeled samples. After panel selection, class-stratified sampling with seed 42 generated a diagnostic training set of 486 and test set of 206. Prognostic modeling separately used 657 complete-survival samples (460 training and 197 testing). Figure S2. Per-gene ROC curves and precision analysis. (a) ROC curves for the 12-gene ElasticNet screening model and individual core biomarkers in the 692 grade-labeled CGGA samples. (b) Precision-recall curve reproduced from the same screening-stage predictions (average precision = 0.771; GBM prevalence = 249/692). Figure S3. Directional expression check in normal brain tissue. Expression of TFRC, TFR2, TRAF6, NCOA4, ALOX15, GCLC, AMD1, and PIK3CB in 8 normal brain samples, 109 LGG samples, and 159 GBM samples from GSE16011. The genes show gene-specific directional patterns, illustrating

that the multigene panel does not rely on a uniform monotonic trend for every component. Figure S4. Ferroptosis module score by IDH status. Single-cell ferroptosis module scores in IDH-wildtype vs. IDH-mutant tumors (Wilcoxon test, $p < 0.001$). Figure S5. Validation. (a) ROC curve of the fixed 12-gene panel in the reproducible CGGA internal test set ($n = 206$; AUC = 0.847, bootstrap 95% CI 0.790–0.896). Upstream discovery preceded the split, so this is not fully independent. (b) ROC curve in GSE16011 ($n = 268$; AUC = 0.775, 95% CI 0.718–0.832). (c) Kaplan–Meier curves in the prognostic CGGA split test set ($n = 197$; HR = 3.95, 95% CI 2.10–7.43). (d) Kaplan–Meier curves in GSE16011 ($n = 224$; HR = 2.08, 95% CI 1.56–2.78; log-rank $p < 0.001$). Figure S6. Ferroptosis gene expression in TAM subpopulations. Dot plot showing the expression of ferroptosis-related genes across tumor-associated macrophage (TAM) subpopulations ($n = 23,839$ cells). Dot size represents the percentage of cells expressing each gene, and color intensity indicates the average expression level.

Author Contributions: M.W. and D.W. conceived and designed the study. M.W. and T.W. performed the bioinformatics analysis and generated the figures. M.W. wrote the original manuscript draft. D.W. supervised the project and revised the manuscript. All authors have read and agreed to the published version of the manuscript.

Funding: This research received no external funding.

Institutional Review Board Statement: Not applicable. This study analyzed only publicly available, de-identified datasets and involved no direct recruitment of human participants or collection of new specimens.

Informed Consent Statement: Not applicable. This study used only publicly available, de-identified datasets.

Data Availability Statement: All datasets analyzed in this study are publicly available. CGGA data were obtained from http://www.cgga.org.cn. The GSE16011 dataset [24] was obtained from the Gene Expression Omnibus (GEO). scRNA-seq data (GSE247824, GSE159416) were obtained from GEO. The complete analysis pipeline is available from the corresponding author upon reasonable request.

Conflicts of Interest: The authors declare no conflicts of interest.

References

1. Ostrom, Q.T.; Price, M.; Neff, C.; Cioffi, G.; A Waite, K.; Kruchko, C.; Barnholtz-Sloan, J.S. CBTRUS statistical report: Primary brain and other central nervous system tumors diagnosed in the United States in 2015–2019. *Neuro Oncol.* **2022**, *24*, v1–v95. [CrossRef]
2. Weller, M.; van den Bent, M.; Preusser, M.; Le Rhun, E.; Tonn, J.C.; Minniti, G.; Bendszus, M.; Balana, C.; Chinot, O.; Dirven, L.; et al. EANO guidelines on the diagnosis and treatment of diffuse gliomas of adulthood. *Nat. Rev. Clin. Oncol.* **2021**, *18*, 170–186. [CrossRef]
3. Cancer Genome Atlas Research Network. Comprehensive, integrative genomic analysis of diffuse lower-grade gliomas. *N. Engl. J. Med.* **2015**, *372*, 2481–2498. [CrossRef]
4. Dixon, S.J.; Lemberg, K.M.; Lamprecht, M.R.; Skouta, R.; Zaitsev, E.M.; Gleason, C.E.; Patel, D.N.; Bauer, A.J.; Cantley, A.M.; Yang, W.S.; et al. Ferroptosis: An iron-dependent form of nonapoptotic cell death. *Cell* **2012**, *149*, 1060–1072. [CrossRef]
5. Jiang, X.; Stockwell, B.R.; Conrad, M. Ferroptosis: Mechanisms, biology and role in disease. *Nat. Rev. Mol. Cell Biol.* **2021**, *22*, 266–282. [CrossRef]
6. Yang, W.S.; SriRamaratnam, R.; Welsch, M.E.; Shimada, K.; Skouta, R.; Viswanathan, V.S.; Cheah, J.H.; Clemons, P.A.; Shamji, A.F.; Clish, C.B.; et al. Regulation of ferroptotic cancer cell death by GPX4. *Cell* **2014**, *156*, 317–331. [CrossRef]
7. Lei, G.; Zhuang, L.; Gan, B. Targeting ferroptosis as a vulnerability in cancer. *Nat. Rev. Cancer* **2022**, *22*, 381–396. [CrossRef]
8. Chen, X.; Kang, R.; Kroemer, G.; Tang, D. Broadening horizons: The role of ferroptosis in cancer. *Nat. Rev. Clin. Oncol.* **2021**, *18*, 280–296. [CrossRef]
9. Cai, Y.; Liang, X.; Zhan, Z.; Zeng, Y.; Lin, J.; Xu, A.; Xue, S.; Xu, W.; Chai, P.; Mao, Y.; et al. A ferroptosis-related gene prognostic index to predict temozolomide sensitivity and immune checkpoint inhibitor response for glioma. *Front. Cell Dev. Biol.* **2022**, *9*, 812422. [CrossRef]
10. Zhuo, S.; Chen, Z.; Yang, Y.; Zhang, J.; Tang, J.; Yang, K. Clinical and biological significances of a ferroptosis-related gene signature in glioma. *Front. Oncol.* **2020**, *10*, 590861. [CrossRef]

11. Zhou, L.; Lu, H.; Zhao, W.; Yu, W.; Chen, S.; Zhang, B.; Li, Z.; Gao, X.; Li, W.; Mao, J.; et al. Robust prediction of glioma prognosis by hypoxia-induced ferroptosis genes: VEGFA-XBP1 co-expression for salvage therapy. *Cancer Biol. Ther.* **2025**, *26*, 2529643. [CrossRef]
12. Hambardzumyan, D.; Gutmann, D.H.; Kettenmann, H. The role of microglia and macrophages in glioma maintenance and progression. *Nat. Neurosci.* **2016**, *19*, 20–27. [CrossRef]
13. Quail, D.F.; Joyce, J.A. The microenvironmental landscape of brain tumors. *Cancer Cell* **2017**, *31*, 326–341. [CrossRef]
14. Klemm, F.; Maas, R.R.; Bowman, R.L.; Kornete, M.; Soukup, K.; Nassiri, S.; Brouland, J.-P.; Iacobuzio-Donahue, C.A.; Brennan, C.; Tabar, V.; et al. Interrogation of the microenvironmental landscape in brain tumors reveals disease-specific alterations of immune cells. *Cell* **2020**, *181*, 1643–1660. [CrossRef]
15. Efimova, I.; Catanzaro, E.; Van der Meeren, L.; Turubanova, V.D.; Hammad, H.; Mishchenko, T.A.; Vedunova, M.V.; Fimognari, C.; Bachert, C.; Coppieters, F.; et al. Vaccination with early ferroptotic cells induces immunogenic cell death-mediated antitumor immunity. *Cell Rep.* **2020**, *32*, 107944.
16. Wang, W.; Green, M.; Choi, J.E.; Gijón, M.; Kennedy, P.D.; Johnson, J.K.; Liao, P.; Lang, X.; Kryczek, I.; Sell, A.; et al. CD8+ T cells regulate tumour ferroptosis during cancer immunotherapy. *Nature* **2019**, *569*, 270–274. [CrossRef]
17. Anandhan, A.; Dodson, M.; Schmidlin, C.J.; Chen, J.; Liu, P.; Wei, Y.; Tan, H.; Wang, Q.; Jiang, Z.; Yang, K.; et al. NRF2 controls iron homeostasis and ferroptosis through HERC2 and VAMP8. *Sci. Adv.* **2023**, *9*, eade9585. [CrossRef]
18. Doll, S.; Freitas, F.P.; Shah, R.; Aldrovandi, M.; da Silva, M.C.; Ingold, I.; Grocin, A.G.; da Silva, T.N.X.; Panzilius, E.; Scheel, C.H.; et al. FSP1 is a glutathione-independent ferroptosis suppressor. *Nature* **2019**, *575*, 693–698. [CrossRef]
19. Neftel, C.; Laffy, J.; Filbin, M.G.; Hara, T.; Shore, M.E.; Rahme, G.J.; Richman, A.R.; Silverbush, D.; Shaw, M.L.; Hebert, C.M.; et al. An integrative model of cellular states, plasticity, and genetics for glioblastoma. *Cell* **2019**, *178*, 835–849. [CrossRef]
20. Ochocka, N.; Segit, P.; Walentynowicz, K.A.; Wojnicki, K.; Cyranowski, S.; Swatler, J.; Mieczkowski, J.; Kaminska, B. Single-cell RNA sequencing reveals functional heterogeneity of glioma-associated brain macrophages. *Nat. Commun.* **2021**, *12*, 1154. [CrossRef]
21. Osorio, D.; Zhong, Y.; Li, G.; Xu, Q.; Yang, Y.; Tian, Y.; Chapkin, R.S.; Huang, J.Z.; Cai, J.J. scTenifoldKnk: An efficient virtual knockout tool for gene function predictions via single-cell gene regulatory network perturbation. *Patterns* **2022**, *3*, 100434. [CrossRef]
22. Eder, M.; Moser, E.; Holzinger, A.; Jean-Quartier, C.; Jeanquartier, F. Interpretable machine learning with brain image and survival data. *BioMedInformatics* **2022**, *2*, 492–510. [CrossRef]
23. Basak, S. Artificial intelligence and machine learning-guided bio-orthogonal engineering of smart soft polymeric nanocarriers for precision drug delivery and translational nanomedicine. *Front. Soft Matter* **2026**, *6*, 1883618. [CrossRef]
24. Gravendeel, L.A.; Kouwenhoven, M.C.; Gevaert, O.; de Rooi, J.J.; Stubbs, A.P.; Duijm, J.E.; Daemen, A.; Bleeker, F.E.; Bralten, L.B.; Kloosterhof, N.K.; et al. Intrinsic gene expression profiles of gliomas are a better predictor of survival than histology. *Cancer Res.* **2009**, *69*, 9065–9072. [CrossRef]
25. Zhou, N.; Bao, J. FerrDb: A manually curated resource for regulators and markers of ferroptosis. *Database* **2023**, *2023*, baad031.
26. Ritchie, M.E.; Phipson, B.; Wu, D.; Hu, Y.; Law, C.W.; Shi, W.; Smyth, G.K. limma powers differential expression analyses for RNA-sequencing and microarray studies. *Nucleic Acids Res.* **2015**, *43*, e47. [CrossRef]
27. Langfelder, P.; Horvath, S. WGCNA: An R package for weighted correlation network analysis. *BMC Bioinform.* **2008**, *9*, 559. [CrossRef]
28. Hao, Y.; Hao, S.; Andersen-Nissen, E.; Mauck, W.M., 3rd; Zheng, S.; Butler, A.; Lee, M.J.; Wilk, A.J.; Darby, C.; Zager, M.; et al. Integrated analysis of multimodal single-cell data. *Cell* **2021**, *184*, 3573–3587. [CrossRef]
29. Kagan, V.E.; Mao, G.; Qu, F.; Angeli, J.P.F.; Doll, S.; Croix, C.S.; Dar, H.H.; Liu, B.; Tyurin, V.A.; Ritov, V.B.; et al. Oxidized arachidonic and adrenic PEs navigate cells to ferroptosis. *Nat. Chem. Biol.* **2017**, *13*, 81–90. [CrossRef]
30. Schonberg, D.L.; Miller, T.E.; Wu, Q.; Flavahan, W.A.; Das, N.K.; Hale, J.S.; Hubert, C.G.; Mack, S.C.; Jarrar, A.M.; Karl, R.T.; et al. Preferential iron trafficking characterizes glioblastoma stem-like cells. *Cancer Cell* **2015**, *28*, 441–455. [CrossRef]
31. Mancias, J.D.; Wang, X.; Gygi, S.P.; Harper, J.W.; Kimmelman, A.C. Quantitative proteomics identifies NCOA4 as the cargo receptor mediating ferritinophagy. *Nature* **2014**, *509*, 105–109. [CrossRef]
32. Gao, M.; Monian, P.; Pan, Q.; Zhang, W.; Xiang, J.; Jiang, X. Ferroptosis is an autophagic cell death process. *Cell Res.* **2016**, *26*, 1021–1032. [CrossRef]
33. Yan, Z.; Garg, S.K.; Kipnis, J.; Banerjee, R. Extracellular redox modulation by regulatory T cells. *Nat. Chem. Biol.* **2021**, *17*, 1158–1166.
34. Walsh, M.C.; Lee, J.; Choi, Y. Tumor necrosis factor receptor-associated factor 6 (TRAF6) regulation of development, function, and homeostasis of the immune system. *Immunol. Rev.* **2015**, *266*, 72–92. [CrossRef]

35. Garg, A.D.; Agostinis, P. Cell death and immunity in cancer: From danger signals to mimicry of pathogen defence responses. *Immunol. Rev.* **2017**, *280*, 126–148. [CrossRef]
36. Fridman, W.H.; Zitvogel, L.; Sautes-Fridman, C.; Kroemer, G. The immune contexture in cancer prognosis and treatment. *Nat. Rev. Clin. Oncol.* **2017**, *14*, 717–734. [CrossRef]

Disclaimer/Publisher's Note: The statements, opinions and data contained in all publications are solely those of the individual author(s) and contributor(s) and not of MDPI and/or the editor(s). MDPI and/or the editor(s) disclaim responsibility for any injury to people or property resulting from any ideas, methods, instructions or products referred to in the content.